

Contents lists available at ScienceDirect

Journal of the Mechanics and Physics of Solids

journal homepage: www.elsevier.com/locate/jmps



Toughness of network materials: Structural parameters controlling damage accumulation



R.C. Picu*, S. Jin

Department of Mechanical, Aerospace and Nuclear Engineering, Rensselaer Polytechnic Institute, Troy, NY, 12180, United States

ARTICLE INFO

Keywords: Fibrous materials Random fiber networks Rupture Damage Toughness

ABSTRACT

Many materials have a network of fibers as their main structural component and are referred to as network materials. Their strength and toughness are important in both engineering and biology. In this work we consider stochastic model fiber networks without pre-existing cracks and study their rupture mechanism. These materials soften as the crosslinks or fibers fail and exhibit either brittle failure immediately after the peak stress, or a more gradual, ductile rupture in the post peak regime. We observe that ductile failure takes place at constant energy release rate defined in the absence of pre-existing cracks as the strain derivative of the specific energy released. The network parameters controlling the energy release rate are identified and discussed in relation to the Lake-Thomas theory which applies to crack growth situations. We also observe a ductile to brittle failure transition as the network becomes more affine and relate the embrittlement to the reduction of mechanical heterogeneity of the network. Further, we confirm previous reports that the network strength scales linearly with the bond strength and with the crosslink density. The present results extend the Lake-Thomas theory to networks without pre-existing cracks which fail by the gradual accumulation of distributed damage and contribute to the development of a physical picture of failure in stochastic network materials.

1. Introduction

The class of network materials includes many engineering and biological materials. These have in common the fact that their mechanical behavior is dictated by an underlaying stochastic network of filaments. Paper, nonwovens, carbon nanotube buckypaper, gels and thermosets are examples of man-made materials, while collagen-based connective tissue, the dermis, the extracellular matrix and the cytoskeleton are biological network materials. While the nature of the filaments (molecules, fibers of several microns diameter, etc.), the nature of the network crosslinks (covalent or ionic bonding between molecules as in molecular networks, mesoscale contacts stabilized by H-bonding as in paper, branching of fiber bundles as in collagen networks), and the presence and type of matrix differ substantially from case to case, the failure of these materials is defined by the way the network ruptures.

The behavior of network materials subjected to uniaxial tension can be divided in two groups: type I networks, which exhibit a yield point followed by softening, and type II, which exhibit hyperelastic response with continuous stiffening. Nonwovens (Patel and Kothari, 2001; Chen et al., 2016) and paper in humid environments (Malho et al., 2015) are of type I, while collagen-based connective tissue and the extracellular matrix are of type II (Ovaska et al., 2017; Meng et al., 2012; Huang et al., 2005; Mauri et al., 2015). Failure is either brittle, case in which catastrophic rupture is not preceded by softening, (Malho et al., 2015; Ovaska et al., 2017) or ductile,

^{*} Corresponding author.

E-mail address: picuc@rpi.edu (R.C. Picu).

case in which pronounced softening occurs before the ultimate loss of load carrying capacity (Chen et al., 2016; Rawal et al., 2013). In the brittle case, the ultimate tensile strength (UTS) coincides with the failure stress, while in the ductile case the UTS corresponds to the peak stress beyond which softening takes place.

The resistance of network materials to fracture is often evaluated using edge cracked samples subjected to tension and the toughness is evaluated using fracture mechanics concepts (Tutwiler et al., 2020; Mao et al., 2017; Stachewicz et al., 2011). Other types of samples adequate for soft materials which deform extensively before the onset of crack growth have been developed in the early works on the mechanical behavior of rubber (Gent and Lindley, 1959; Gent and Tobias, 1982; Lake and Lindley, 1964, 1965). Many soft network materials, including collagen-based connective tissue (Oyen et al., 2004; Purslow, 1985; Stok and Oloyede, 2007) and double network gels (Li et al., 2014; Mai et al., 2018) are remarkably tough. Gels with toughness above $10,000 \ J/m^2$ have been reported (Li et al., 2014). On the other hand, densely crosslinked networks composed from stiff filaments, such as paper in dry environment (Alava and Niskanen, 2006; Popil, 2017) and networks of ceramic fibers (Shi et al., 2020) have low toughness of values close to $1 \ J/m^2$. The extreme difference between these two types of materials is due to the fact that soft networks sustain large deformations and fibers realign in the vicinity of the crack tip in the direction orthogonal to the crack plane, therefore providing large resistance to crack growth (Koh et al., 2013). Due to this network reorganization, very large crack opening displacements are possible and the process zone at the crack tip may grow to dimensions comparable with the sample size. Under such conditions, the stress concentration effect of the pre-existing crack is drastically reduced and the network ruptures at a local stress which is comparable to the UTS of the virgin sample.

In molecular networks, the toughness is typically rationalized based on the Lake-Thomas model (Lake and Thomas, 1967) which relates the energy release rate, G, to molecular network parameters. Specifically, this model indicates that G is proportional to the crosslink or molecular filament strength, the density of filaments crossing the crack plane, and the difference between the contour length of the filament between crosslinks and its equilibrium end-to-end length. An equivalent model applicable to cases without pre-existing cracks and in which damage accumulates gradually before the final failure is not available. Taking steps in this direction is the central goal of the present work.

Most works focusing on the failure of network materials without pre-existing cracks report the UTS, but not the toughness. Experimentally, UTS was observed to increase approximately linearly with increasing network density (total length of fiber per unit volume, in 3D, or area, in 2D) (Alava and Niskanen, 2006; Fukasawa et al., 2010; Eriksson et al., 2006) or the crosslink density (Normand et al., 2000; Fang and Li, 2012). If the crosslink density scales linearly with the network density, the two parameters become equivalent for the purpose of UTS evaluation. A small number of attempts have been made to measure the strength of the inter-fiber bonds and to relate this parameter with the UTS of the respective networks. The only reports along these lines that seem to be available at this time are related to cellulose networks (Eriksson et al., 2006; Forsstrom et al., 2005). It is concluded that UTS scales linearly with the mean crosslink strength. Support for the idea that UTS is proportional to the crosslink density and with the crosslink strength was also provided by several computational works (Heyden, 2000; Heyden and Gustafsson, 1998; Borodulina et al., 2012; Borodulina et al., 2018; Goutianos et al., 2018; Deogekar and Picu, 2018; Deogekar et al., 2019). It was also concluded that the fiber mechanical behavior or fiber tortuosity have little to no effect on UTS (Deogekar et al., 2019). These models also indicate that the fraction of crosslinks (or fibers) that fail before the peak stress is small (about 5%) and, at peak stress, either a major crack nucleates and grows leading to brittle failure, or a diffuse damage process sets in leading to gradual softening.

Structural stochasticity favors the accumulation of diffuse damage. If network parameters are such that deformation is non-affine (low density and/or thin filaments that deform preferentially in the bending mode), (Head et al., 2003; Heussinger and Frey, 2006; Hatami-Marbini and Picu, 2008; Picu, 2011) local strains are different from the global, imposed strains, the energy and stress fields are highly fluctuating spatially, and hence damage may occur locally even at small applied global deformations. However, structural stochasticity has a stabilizing effect on the nucleated damage and hence promotes ductile deformation (Deogekar and Picu, 2018; Deogekar et al., 2019). Enhanced stochasticity in the vicinity of stiffness percolation (in these works the system is maintained in the vicinity of the critical point by controlling the mean network connectivity, z) was shown to lead to ductile behavior (Berthier and Kollmer, 2019; Zhang and Rocklin, 2017). Fracture in heterogeneous materials was studied by the mechanics (Bazant et al., 1991; Waddoups et al., 1971) and statistical physics (Herrmann et al., 1981; Malakhovsky and Michels, 2007) communities. Most studies in the physics literature were performed using the random fuse (Arcangelis et al., 1989; Hansen et al., 1991) or random spring networks (Alava et al., 2008; Jagota and Bennison, 1994). These networks do not undergo large deformations and retain their initial geometry as damage evolves. Effects such as intermittency (Bonamy, 2009; Rosti et al., 2009) and the competition between distributed damage and localization (Alava et al., 2008; Isaksson and Hägglund, 2007) are observed. In models with pre-existing cracks, crack pinning, (Daguier et al., 1997; Rosti et al., 2001) crack path roughening (Roux et al., 2003) and strong size effects (Herrmann et al., 1981; Malakhovsky and Michels, 2007; Curtin, 1998) are observed. These works create a conceptual framework within which some aspects of the network materials failure can be understood, but do not account for the complexities associated with large deformations, strong geometric non-linearities and the intrinsic structural and mechanical heterogeneity of the network.

The objective of this work is to explore the gradual failure process in the post peak regime. We consider athermal networks of large free volume, which are not embedded in matrix and in which damage is due to crosslink failure. We observe that the gradual rupture in the post peak regime takes place at constant energy release rate and identify the controlling network parameters. We also observe a transition from ductile to brittle behavior as the degree of non-affinity and the effective mechanical heterogeneity of the network decrease. The models, methods and parameters of interest are described in Section 2. The effect of the crosslink strength on the failure process is discussed in Section 3.1 and the structural parameters defining the UTS are reviewed in Section 3.2. The relation between the degree of non-affinity and network brittleness is presented in Section 3.3, while the analysis of the energy release rate is presented in

Section 3.4. The conclusions of the work are summarized in Section 4.

2. Models, methods, and parametric space

2.1. Models and parameters

Stochastic athermal networks of Voronoi type are considered in this work. These are generated by defining in a cubic volume of edge size L a number of randomly positioned seed points. The volume is tessellated with the Voronoi procedure based on the seed points and the edges of the tessellation are retained as fiber segments, Fig. 1a. The network density, ρ , i.e. the total length of fiber per unit volume, is controlled by varying the density of seed points. The resulting fiber segments have no preferential orientation and are straight in the undeformed configuration. The connectivity number, z, represents the number of segments merging at a crosslink and is z=4 in the bulk of the Voronoi network. The length of fiber segments is Poisson distributed and the mean fiber segment length, l_c , is related to the density as $\rho l_c^2 \approx 0.95$; this non-dimensional group takes different values if the Voronoi structure is perturbed stochastically (Deogekar et al., 2019). Voronoi networks resemble cellular structures with open cells (Jang et al., 2008) and have been used extensively to represent fibrous materials (Zhang et al., 2013; Shulmeister et al., 1998; Picu et al., 2018; Amjad and Picu, 2022).

Given that four fiber segments meet at each crosslink, it is possible to view the crosslink as a bond connecting two continuous fibers, as done in (Deogekar and Picu, 2018; Deogekar et al., 2019) and (Deogekar and Picu, 2021). To define fibers composed from multiple fiber segments, the network is decomposed in paths that traverse the structure. The paths are truncated at a length $L_0 \approx 4l_c$ and each path becomes a fiber having, in average, 4 non-colinear but contiguous segments, which are the edges of the Voronoi tessellation. The procedure of breaking continuous paths across the network into fibers of finite length reduces the average connectivity of the network which, including the effect of surfaces, becomes $\langle z \rangle = 3.15$.

The crosslinks are represented by connectors of high stiffness which transmit both forces and moments between fibers. The connectors are characterized by axial and bending stiffnesses, K_b^f and K_b^m , such that the force and moments transmitted are related to the relative displacements, Δu_i , and rotations, $\Delta \theta_i$, of the respective fibers at the contact point as $F_{bi} = K_b^f \Delta u_i$ and $M_{bi} = K_b^m \Delta \theta_i$, with i = 1, 2, 3 representing the 3 directions of a local coordinate system tied to the crosslink, x_{bi} (Fig. 1b), and having axis x_{b3} aligned with the connector. A physical model of the crosslink between fibers and its failure is presented in Deogekar and Picu (2018) and used here. In this view, a crosslink between two fibers is established by many small parallel fibrils, Fig. 1b. Failure of the crosslink in the opening and shear modes requires the simultaneous rupture of all these fibrils. Failure of the crosslink due to the relative fiber rotation, i.e. in the rolling or peeling mode, requires the gradual rupture of the fibrils. Such representation is supported by observations in cellulose networks (Heyden and Gustafsson, 1998; Schmied et al., 2013) in which nanoscale fibrils connect cellulose microfibers at inter-fiber contacts, and in collagen, e.g. (Sherman et al., 2015), where fibers have multiscale structure and are actually bundles of smaller scale fibrils. The connector used in the present models represents all the fibrils that may be present at a crosslink.

This model leads to a failure criterion of the form $F_{eq} = f_c$, where f_c is a characteristic parameter of the crosslink referred to as the bond strength, and $F_{eq}^2 = F_{b1}^2 + F_{b2}^2 + \langle F_{b3} - \frac{6}{d} \sqrt{M_{b1}^2 + M_{b2}^2} \rangle^2$ is the equivalent applied force (Deogekar and Picu, 2018; Deogekar et al., 2019; Deogekar and Picu, 2021). The force in the x_{b3} local direction, F_{b3} , is reduced by the effect of the rotation of the fibers relative to

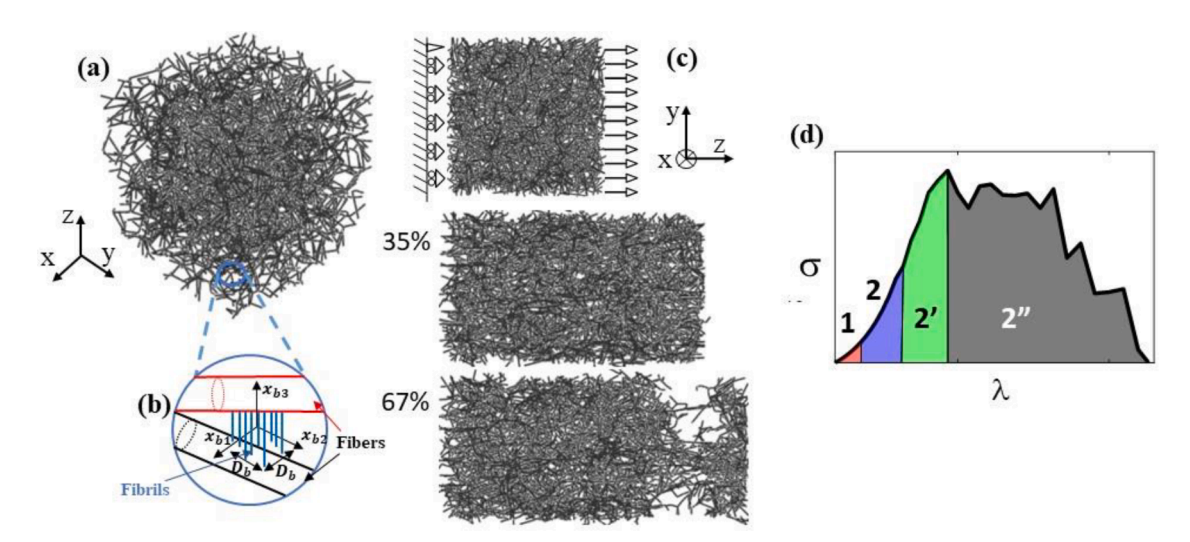


Fig. 1. (a) Realization of a 3D network and (b) detail of the geometry at a crosslink including the local coordinate system x_{bi} . The blue parallel lines represent the crosslink composed from multiple fibrils connecting two fibers (shown in black and red). The connector used to model the crosslink represents all fibrils forming the respective crosslink. (c) Boundary conditions and deformed configurations of the network. (d) Schematic representation of the 4 deformation regimes discussed in text.

each other since rupture of the crosslink requires the rupture of all fibrils, some of which are being compressed during fiber rolling. The effective rolling moment, $\sqrt{M_{b1}^2 + M_{b2}^2}$, is divided by a length equal to the size of the contact spot, D_b , which is taken here equal to d/6, where d is the fiber diameter. <> indicates the Macaulay bracket, which vanishes if the quantity in the bracket is negative and is equal to the respective quantity when it is positive. While the crosslink has finite torsional stiffness, it is assumed here to not fail in pure torsion and hence M_{b3} does not appear in the failure criterion. The equivalent relative displacement of the two fibers forming the crosslink, Δu_{eq} , is related to the equivalent force in the crosslink, as discussed in Deogekar and Picu (2018), and it reaches a critical value, u_c , at crosslink failure.

Crosslink failure has been modeled in other works using the cohesive zone model (Goutianos et al., 2018; Kulachenko and Uesaka, 2012) using connectors that rupture at a specific transmitted force or specific combination of transmitted force and moment (Bergstrom et al., 2019). Provided the crosslink stiffness is not too low, the crosslink deformation is minimal compared to the deformation of the fibers and a force-based criterion for crosslink failure is appropriate. This was emphasized in Chen et al. (2016) where cohesive zone elements were used to represent crosslink failure. An energy-based criterion is considered more adequate when the crosslink stiffness is low (Borodulina et al., 2012; Goutianos et al., 2018).

The fiber material is considered linear elastic, of Young's modulus E_f and Poisson ratio ν_f . The Poisson ratio of fibers, ν_f , is of little importance in the behavior of the network. Fiber plasticity is ignored since in networks of large free volume whose deformation is non-affine, as considered here, the strain in fibers is unlikely to reach the yield strain; the ratio between the strain at which fibers reach yielding to the strain at which the network yields in non-affine athermal networks with elastic-plastic fibers is proportional to the fiber aspect ratio, d/l_c (Picu, 2022). The situation is opposite in dense and densely crosslinked networks, where the fiber strain is, by definition, approximately equal to the far field strain. When low density, non-affinely deforming networks are observed experimentally to deform plastically, the apparent plasticity is actually due to fiber rearrangements and to inter-fiber contacts and friction. While network rearrangement and large geometric nonlinearity are accounted for in the present models, friction at inter-fiber contacts is not captured and hence, in the absence of damage, these networks have reversible mechanical behavior.

The primary structural parameters used to characterize the network are the density, ρ , the fiber diameter, d, and the crosslink strength, f_c . Parameters derived from the primary ones are the mean length of a segment between crosslinks, l_c ($l_c = 0.95 / \sqrt{\rho}$ for the Voronoi network, as indicated above), the crosslink density, ρ_b , which is related to the other parameters through the geometric relation

$$\rho = \rho_b \bar{z} l_c / 2,$$
(1)

and the effective crosslink deformation at crosslink failure, u_c , which is related to f_c via the crosslink stiffness. Here, \bar{z} is the average connectivity number.

The nondimensional parameter ρd^2 (also written as $w = log_{10}(\rho d^2)$) plays an important role in the mechanics of stochastic networks as it controls the transition from affine to non-affine behaviors (Deogekar and Picu, 2018; Head et al., 2003; Islam and Picu, 2018). Specifically, for Voronoi networks, when w > 1, the deformation is affine, the strain energy is stored primarily in the axial deformation mode of fibers and the small strain modulus, E_0/E_f , is proportional to ρd^2 . For w < -1, deformation is non-affine, with the degree of non-affinity increasing as w decreases, the strain energy is stored predominantly in the bending deformation mode of fibers and E_0/E_f is proportional to $\rho^2 d^4$ (see e.g. the master plot relating E_0/E_f to w in (Deogekar and Picu, 2018; Islam and Picu, 2018)). A transition regime between these two types of behavior takes place in the approximate range -1 < w < 1. In an affinely deforming network, the strain and energy distributions are spatially uniform, while in a non-affine network these parameters have large spatial fluctuations. Therefore, while the affine networks behave mechanically similar to homogeneous materials despite their geometric heterogeneity, non-affine networks are mechanically heterogeneous. In this sense, parameter w controls the degree of mechanical heterogeneity of the network. Note that d/l_c represents the slenderness ratio of the mean segment, which is related to w as $w \approx 2log_{10}(d/l_c)$ for these networks.

In this work, the density was varied by a factor of 3, d was varied by 3 orders of magnitude and f_c was varied by 5 orders of magnitude. This corresponds to w ranging from -3.84 to -0.82, i.e. spanning the non-affine regime and into the transition between the non-affine and affine regimes.

2.2. Simulation parameters and methods

The fiber segments (bounded by 2 consecutive crosslinks) are represented with one three-nodes Timoshenko beam element (B32) and hence a fiber is modeled with 4 such elements, in average. The model is loaded in uniaxial tension, Fig. 1c, by imposing displacements on two opposite faces, while keeping the other 4 faces traction free. The model is free to contract in the directions orthogonal to the loading direction, including at the two surfaces where displacements in the loading direction are prescribed.

The crosslinks are represented using the connector element CONN3D2 and the connector section BUSHING in Abaqus, which allow controlling independently the translational and rotational stiffnesses of the crosslinks. The forces and moments transmitted by the connector are determined from the solution and the connector is allowed to separate when the failure condition $F_{eq} = f_c$ is fulfilled.

The solution is obtained with the commercial finite element solver Abaqus/Explicit, version 62.3. Dynamic and inertial effects occur with the solution scheme used, particularly after the onset of crosslink rupture. We use a numerical damping scheme (bulk viscosity) to minimize this effect. The loading rate is reduced after the onset of crosslink rupture and damping is adjusted such to maintain the kinetic energy of the model lower than 1% of the total energy prior to the onset of cross-link failure, and lower than 5% of the total energy after the peak stress. This ensures that the simulation is approximately quasi-static in each case considered. The

simulation provides the total force applied as a function of stretch and this is used to compute the nominal (first Piola-Kirchoff) stress. The nominal stress is used here since this is the parameter usually measured in experiments. Three replicas (different geometric configurations of the network) are considered for each case and the plots represent the average respective quantity at the given stretch.

3. Results

3.1. Effect of the bond strength

The uniaxial deformation of network materials without matrix has been discussed extensively in the literature, see (Picu, 2022) for a review. Here we work with the nominal stress (first Piola-Kirchoff normal stress component in the loading direction, S) and the stretch, λ , which form a pair of work conjugate parameters. A typical stress-stretch curve of type II networks (as those studied here), in the absence of damage accumulation, may be divided into 3 regimes. Regime 1 is linear elastic, of small strain stiffness E_0 , and extends to about 2-3% strain. This regime may not be visible in experiments with very soft samples as the forces required for deformation in regime 1 may fall below the resolution limit of the load cell. The material stiffens exponentially in regime 2, i.e. the nominal tangent stiffness (computed as the derivative of the nominal stress with respect to the strain) is proportional to the stress, while in regime 3 the stiffening rate decreases and the nominal tangent stiffness is approximately proportional to the square root of the stress, see e.g. (Licup et al., 2016; Zagar et al., 2015).

If crosslinks are allowed to rupture, the stress-stretch curve exhibits a peak after which continuous softening is observed. The stress corresponding to the peak (UTS) may be controlled by increasing the crosslink strength, f_c . Fig. 2a shows $S(\lambda)$ curves for strongly non-affine models with w=-3.84 and four values of the normalized bond strength, $f_c/(E_fd^2)$, ranging from 1.1×10^{-3} to 7.6×10^{-3} . The corresponding stress-stretch curve for the same type of network in which crosslinks do not rupture is shown with dashed red line in Fig. 2a.

The curves corresponding to different f_c values overlap for the most part of the pre-peak segment and exhibit little variability. The UTS increases with increasing f_c , as previously reported (Heyden and Gustafsson, 1998; Borodulina et al., 2018; Goutianos et al., 2018; Deogekar and Picu, 2018; Deogekar et al., 2019). The decay of the stress beyond the peak occurs at rates which appear to scale with

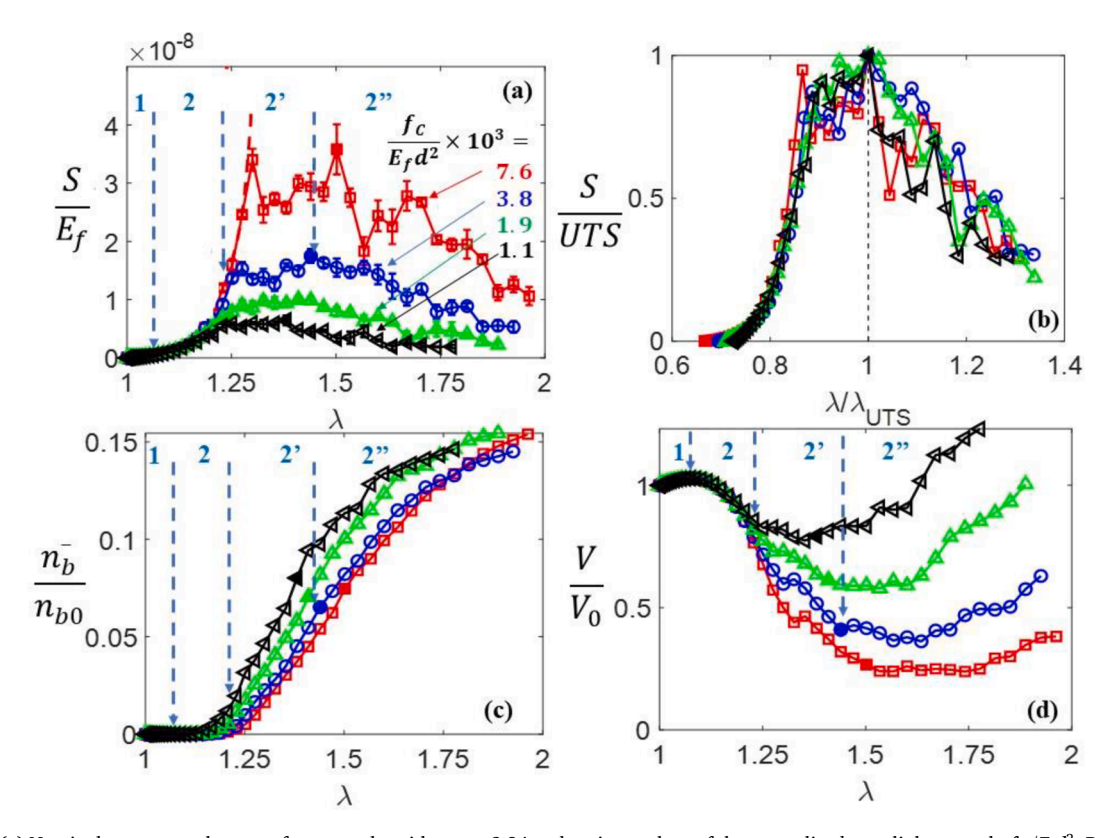


Fig. 2. (a) Nominal stress-stretch curves for networks with w=-3.84 and various values of the normalized crosslink strength, f_c/E_fd^2 . Regimes 1, 2, 2' and 2" described in the text are shown for the (blue, circle symbols) curve with $f_c/E_fd^2=3.8\times10^{-3}$. (b) Data in (a) shown after the normalization of the vertical axis with the UTS and of the horizontal axis with the stretch at peak stress, λ_{UTS} . Variation of (c) the fraction of failed crosslinks and (d) relative sample volume during deformation for all cases shown in (a). The transition between regimes 2' and 2" corresponds to the peak stress, and approximately to the minimum volume and the inflection point of the n_b/n_{b0} curve, as shown for the curves marked by circle symbols.

UTS. In other words, the functional form of the softening regime appears to be independent of f_c . This is demonstrated in Fig. 2b, where the curves in Fig. 2a are shown after normalization of the vertical axis with UTS and of the horizontal axis with the stretch at the peak, λ_{UTS} . The normalization removes the overlap in the pre-peak regime but allows the post-peak branches to come together.

Four regimes of deformation may be identified and are marked with vertical dashed lines in Fig. 2 for the curve with f_c / $E_f d^2 = 3.8 \times 10^{-3}$. The regimes are also shown schematically in Fig. 1d. Regimes 1 and 2 are identical to those of the network without failure, i.e. regime 1 is linear elastic and exponential stiffening is observed in regime 2. Regime 2' spans from the onset of crosslink failure to the peak stress, while regime 2' is the post peak regime.

Fig. 2c shows the variation during deformation of the fraction of ruptured crosslinks, n_b/n_{b0} , where n_b is the number of failed crosslinks and n_{b0} is the number of crosslinks of the initial, unloaded structure. n_b/n_{b0} is zero in the pre-peak regimes 1 and 2 and starts to increase at the beginning of regime 2'. The fraction of broken crosslinks at peak stress is in the range 5 to 7%. The peak stress corresponds approximately to the inflection point of the n_b/n_{b0} curve. The $n_b/n_{b0}(\lambda)$ curves are similar, although slightly translated in the horizontal direction due to the different onset stretch of crosslink rupture in systems with different f_c . The fact that the rate at which crosslinks rupture is independent of f_c is the mechanistic cause of the overlap of the stress-strain curves in the post-peak regime seen in Fig. 2b.

 n_b/n_{b0} reaches values as high as 15%, which is close to the value of bond percolation on the Voronoi lattice, reported in Jerauld et al. (1984) to be 14.53%. This match is likely coincidental since bond percolation corresponds to the formation of percolated paths of failed crosslinks across the network, while full brittle failure requires the formation of an entire plane of ruptured bonds that traverses the network and separates the material in two parts. The emergence of such a plane through an entirely stochastic process takes place at much larger fractions of failed crosslinks (above 80%) (Pal and Picu. 2017).

The variation of the sample volume V (normalized by the initial volume of the unloaded state, $V_0 = L^3$) during deformation is shown in Fig. 2d. The volume increases in regime 1, as expected for a linear elastic material with no damage. The effective Poisson ratio of the network in this regime is \sim 0.4. The network undergoes no structural changes at these small strains. The onset of the stiffening regime 2 is associated with internal instabilities that allow structural evolution. This causes an increase of the incremental Poisson ratio which may reach values as large as 6 in the absence of damage, as discussed previously (Picu et al., 2018) (the incremental Poisson ratio relative to the stretch direction in uniaxial loading is computed based on the true strain as $v_i = -d \ln \lambda_{\perp}/d \ln \lambda$, where λ and λ_{\perp} are stretches in the imposed deformation direction and perpendicular to it, respectively). This dramatic increase of the Poisson ratio was observed in experiments with collagen-based membranes (Mauri et al., 2015) and in felt (Kabla and Mahadevan, 2007). Therefore, the volume of the network decreases rapidly in regime 2. This trend continues in regime 2', but at lower rate since crosslink rupture allows the structure to relax. V/V_0 increases in regime 2'; this is somewhat an artifact of the way the volume is computed; the large pores that open within the network in regime 2' are still considered to be part of the network volume (see also Fig. 1c). This phenomenology is observed consistently for all f_c . The incremental Poisson ratio increases during regime 2' followed by a rapid decrease during regime 2", which is also observed in experiments if damage accumulation occurs (Kabla and Mahadevan, 2007; Bancelin et al., 2015).

3.2. Parameters controlling the strength

The relationship between network strength and the geometric and material parameters was discussed in the literature (Borodulina et al., 2018; Goutianos et al., 2018; Deogekar and Picu, 2018, 2021; Kulachenko and Uesaka, 2012). Here we outline a simple mean field explanation that leads to a structure-property relation of this type and show that the present dataset supports the respective conclusion.

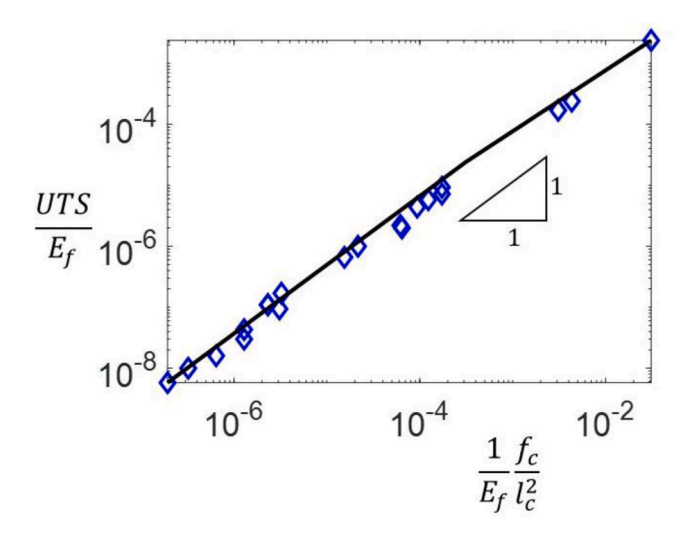


Fig. 3. Nominal network strength vs. f_c/l_c^2 for the entire range of parameters considered in this study.

Assuming that the force carried by the crosslinks, f, in a loaded equilibrium state is Poisson distributed with mean \bar{f} and probability distribution $p(f) = (1/\bar{f}) \exp(-f/\bar{f})$, it is possible to evaluate the fraction of crosslinks loaded above their strength f_c ; this fraction

becomes $\int_{f_c}^{\infty} p(f)df = \exp(-f_c/\bar{f})$. According to the data in Fig. 2c, the peak stress is reached when this fraction becomes equal to a

constant, $\beta \approx 0.05$. Hence, when the peak stress is reached, the relation $\bar{f} = f_c/(-\ln\beta)$ must hold. The nominal stress may be computed, in the mean field sense, as the mean force per crosslink divided by the area corresponding to a crosslink projected in the plane orthogonal to the loading direction in the reference configuration: $S = \bar{f} \rho_b l_c$ (assuming that the mesh size is equal to the mean segment length, as is the case for the networks considered here). Therefore, one may use the expression for the mean force \bar{f} corresponding to the peak stress to evaluate the strength:

$$UTS \sim f_c \rho_b l_c.$$
 (2)

This expression can be rewritten using Eq. (1) and the relationship between ρ and l_c as $UTS \sim f_c \rho \sim f_c / \ell_c^2$.

Fig. 3 shows the relation between UTS and f_c/l_c^2 , both quantities being normalized by E_f , for all 22 network types considered in this study, and for the entire range of f_c , d and ρ mentioned in section 2, and w ranging from -3.84 to -0.82. The figure provides strong support for the linear scaling of the strength with f_c/l_c^2 . The coefficient of proportionality in $UTS \sim f_c/l_c^2$ resulting from Fig. 3 is 0.09.

Simulations of fiber networks that fail at small strains by Heyden (2000) indicate linear scaling of the strength with the density, provided the density is significantly larger than the stiffness percolation threshold. Models of paper reported in Borodulina et al. (2012) indicate an approximate linear relation between strength and the crosslink density. UTS is reported in Goutianos et al. (2018) to scale linearly with f_c and somewhat sublinearly with ρ_b . Experimental proof of linear scaling of UTS with network density (concentration of molecular component forming the network) is provided in Fukasawa et al. (2010), Normand et al. (2000) for PEG gels, as well as in Eriksson et al. (2006) for cellulose networks (paper), and in Chen et al. (2016) for polymeric fiber nonwovens. Works with cellulose networks (Eriksson et al., 2006; Forsstrom et al., 2005) show that the strength of paper scales linearly with the crosslink strength, which was measured separately in dedicated experiments for the same samples.

3.3. Brittle to ductile transition

A significant change of network behavior results by changing w. Fig. 4a shows nominal stress-stretch curves for networks with w = -3.84, -2.84 and -0.82. The first two cases are strongly non-affine, while the third case is in the transition to affine deformation. The variation of w is achieved here by keeping the density constant and increasing the fiber diameter, d. To maintain the stability of the simulation, f_c is also increased in approximate proportion with d^2 . The non-affine networks are much softer than the close-to-affine one

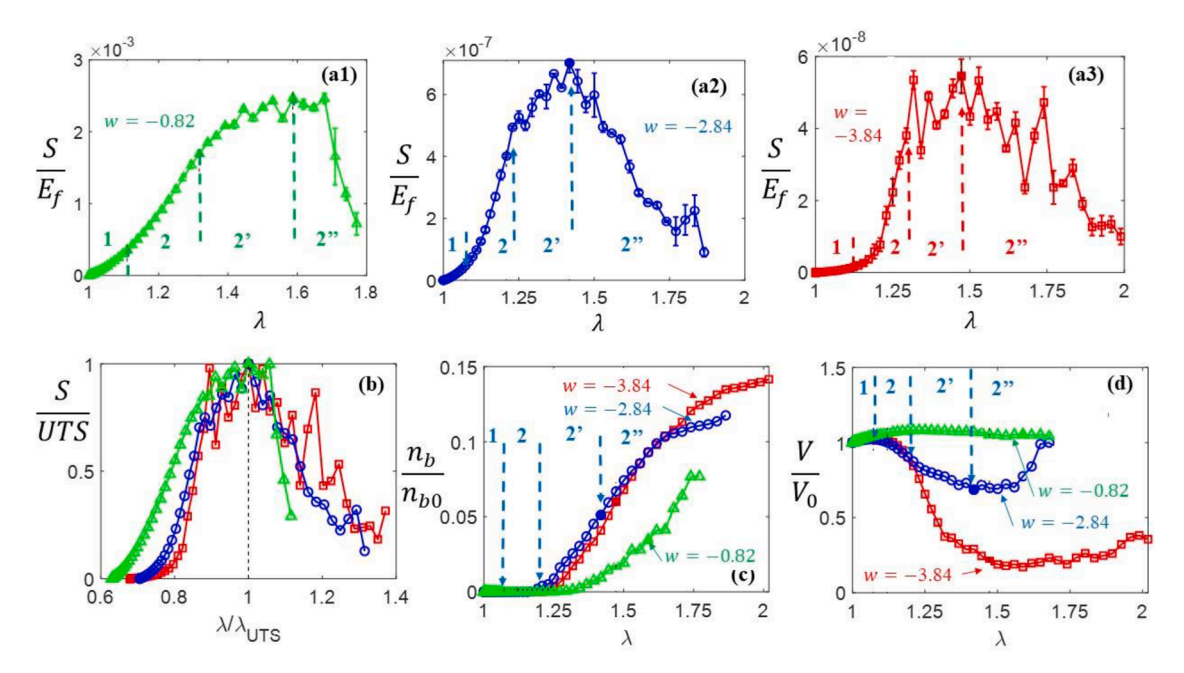


Fig. 4. (a) Nominal stress-stretch curves for networks with (a1) w = -0.82, (a2) w = -2.84 and (a3) w = -3.84. Regimes 1, 2, 2' and 2" described in text are shown for all curves in (a) and for the case with w = -2.84 in (c) and (d). (b) Data in (a) after the normalization of the vertical axis with the UTS and of the horizontal axis with the stretch at peak stress. Variation of (c) the fraction of failed crosslinks and (d) sample volume during deformation for all cases shown in (a).

and exhibit the hyperelastic behavior described in section 3.1. However, the important observation is that the stretch at failure relative to the stretch at peak stress decreases as w increases, and the network with w = -0.82 exhibits rapid failure right after the peak stress. This behavior is shown more clearly in Fig. 4b, where the data in Fig. 4a is replotted after the normalization of the vertical axis by UTS and of the horizontal axis by the stretch at the peak, λ_{UTS} . This shows that the behavior becomes more brittle as the degree of non-affinity of the network decreases. Since f_c has no effect on the functional form of the post-peak segment of the stress-stretch curve (Fig. 2b), the ductile to brittle transition is associated here with the increase of w.

Fig. 4c shows the variation of the fraction of ruptured crosslinks, n_b/n_{b0} , for the three cases. The 4 regimes identified in Fig. 2 are shown in panels (c) and (d) of Fig. 4 for the network with w = -2.84. The n_b/n_{b0} curves differ significantly from those shown in Fig. 2c. The non-affine networks sustain the rupture of twice as many crosslinks before they lose the load carrying capacity compared with the more affine network with w = -0.82.

Fig. 4d shows the variation of the normalized sample volume. While the non-affine networks exhibit the strong volume reduction also observed in Fig. 2d, the network with w = -0.82 shows little volumetric variation in regimes 2 and 2'. This network has no regime 2" since it fails abruptly after the peak stress. The lack of contraction is due to the inability of the close-to-affine network to rearrange during straining; it exhibits a long regime 1 and weak stiffening in regime 2.

Ductile to brittle transitions are observed in both experiments and simulations. Driscoll et al. (2016) report simulations of spring lattices with disorder and observe that the behavior becomes more brittle as the fiber and/or crosslink density increases and the non-affinity of the deformation decreases. The ductility may be also controlled by adjusting the degree of sample confinement which, in turn, modifies the degree of non-affinity of the deformation field. Increasing confinement may be achieved either by increasing the network size or by applying restrictive boundary conditions. A size-induced ductile to brittle transition is reported in, (Dussi et al., 2020) with the rupture becoming more brittle as the network size increases. A similar reduction of the strain at failure with increasing model size is reported in Kulachenko and Uesaka (2012).

3.4. Energy release rate

We analyze further the energy released as the network ruptures in the post-peak regime. To this end, we compute first the energy released per crosslink failure, U_{rpb} , as the negative of the variation of the potential energy over a stretch increment divided by the number of crosslinks that rupture in the same stretch interval. U_{rpb} is then normalized by the product $f_c u_c$, which is the work required to break one crosslink on the local scale. The normalized energy released per crosslink, $U_{rpb}/f_c u_c$, is shown in Fig. 5a for all networks with w=-3.84 considered in Fig. 2. These networks have same ρ and d, but different f_c . The figure shows that the energy released per crosslink failure increases during deformation.

The energy released per crosslink failure is much larger than the work required to break one crosslink, $U_{rpb} \gg f_c u_c$. This implies that most of the energy released is stored strain energy and little is consumed to rupture the crosslinks. This is similar to crack growth in ductile metals, where most of the energy is dissipated and only a small fraction corresponds to the creation of new free surfaces. In the current problem there is no plastic dissipation; however, the strain energy released when a crosslink rupture is recovered as network vibrations, which are then damped by the algorithmic damping that ensures that the simulation remains quasistatic. This mesoscale dissipation mechanism is equivalent to nanoscale dissipation by heat production. In a physical network, damping is provided either or both by fiber-fiber friction (e.g. in polymeric networks of low free volume such as molecular networks above the glass transition temperature) and the interaction of fibers with a fluidic matrix (e.g. in polymeric networks of large free volume such as gels).

It is further possible to compute the volume of the network from which the energy released per crosslink failure is extracted as $v_{rpb} = VU_{rpb}/SE$, where $V = V(\lambda)$ is the current volume of the sample (Fig. 2c) and $SE = SE(\lambda)$ is the strain energy stored in the entire sample

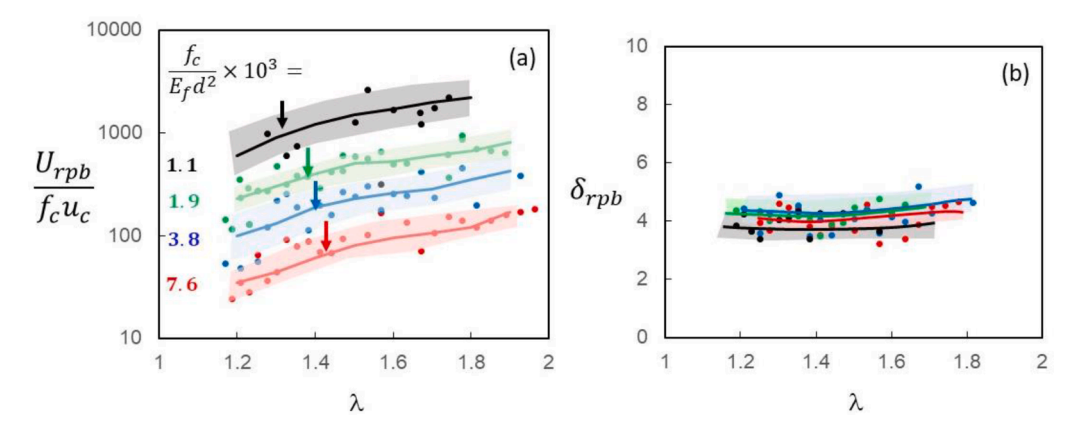


Fig. 5. (a) Variation of the energy released per crosslink failure, U_{pb} , normalized by the work required to separate a crosslink, $f_c u_c$, during regimes 2' and 2" of all networks shown in Fig. 2. The arrows indicate the position of the peak stress. (b) Diameter in the current configuration of a network subdomain containing strain energy equal to the energy released per crosslink failure, expressed in units of l_c . The legend in (a) applies to both panels. The points represent values obtained with one realization, the shades show the range of fluctuations, and the lines show the means.

(SE/V) is the mean strain energy density). The size of such subdomains expressed in multiples of l_c is $\delta_{rpb} = v_{rpb}^{1/3}/l_c$. This quantity is shown in Fig. 5b for all networks considered in Fig. 5a. It is observed that for these networks $\delta_{rpb} \approx 4$, which is independent of f_c and is constant during deformation. Hence, the energy released per crosslink failure is equivalent to the strain energy stored in a network domain surrounding the respective crosslinks having diameter $\sim 4l_c$.

The energy release rate is well-defined in fracture mechanics as the energy released per unit crack front length and unit crack advance. In the present situation, when no pre-existing cracks are present, we define the specific energy release rate, G^s , as the energy released per strain increment and per unit volume. This quantity is evaluated based on the mean energy released per crosslink failure, U_{mh} , and the rate of crosslink rupture, $dn_h/d\lambda$:

$$G^{s} = \frac{1}{V} \frac{dn_b}{d\lambda} U_{rpb} \tag{3}$$

We emphasize the difference between the fracture mechanics energy release rate, G, and the present measure, G^s : G represents the energy released per unit crack advance and unit crack front length, while G^s is the energy released per unit stretch increment and per unit volume in the current configuration. Both are energy release rates in the sense that the control parameter in the fracture mechanics case is the crack length, while in the present case of diffuse damage, the control parameter is the applied stretch. The units of the two quantities are different, by definition: while G has units of J/m^2 , G^s has units of J/m^3 . In a generalized deformation situation, G^s may be defined as the derivative of the energy released with respect to the curvilinear coordinate in strain space along the deformation path, and per unit volume in the current configuration.

Fig. 6a shows the values of G^s corresponding to all systems considered in Fig. 2, where G^s is rendered non-dimensional by normalization with E_f (E_f is identical for all models). Fig. 6b shows the same data after normalization of G^s with f_c / I_c^2 . The equivalent data for the systems of different w shown in Fig. 4 is presented in Fig. 6c and d.

The specific energy release rate increases initially and remains approximately constant for the most part of the regime in which crosslinks rupture gradually (diffuse damage accumulation). The values of G^s in the various systems considered is very different, particularly when both w and f_c are varied. However, the normalization of G^s with f_c/l_c^2 leads to the collapse of the curves, Fig. 6b and d. Therefore, it is possible to infer that $G^s \sim f_c/l_c^2 \sim UTS$, where the second relation is based on the data in Fig. 3. In the case of the brittle system with w = -0.82, G^s corresponding to the last increments when the structure fails (not shown in Fig. 6c) is orders of magnitude larger than the specific energy release rate recorded before catastrophic failure.

As in fracture mechanics, one may consider that gradual rupture takes place when the energy release rate becomes equal to the

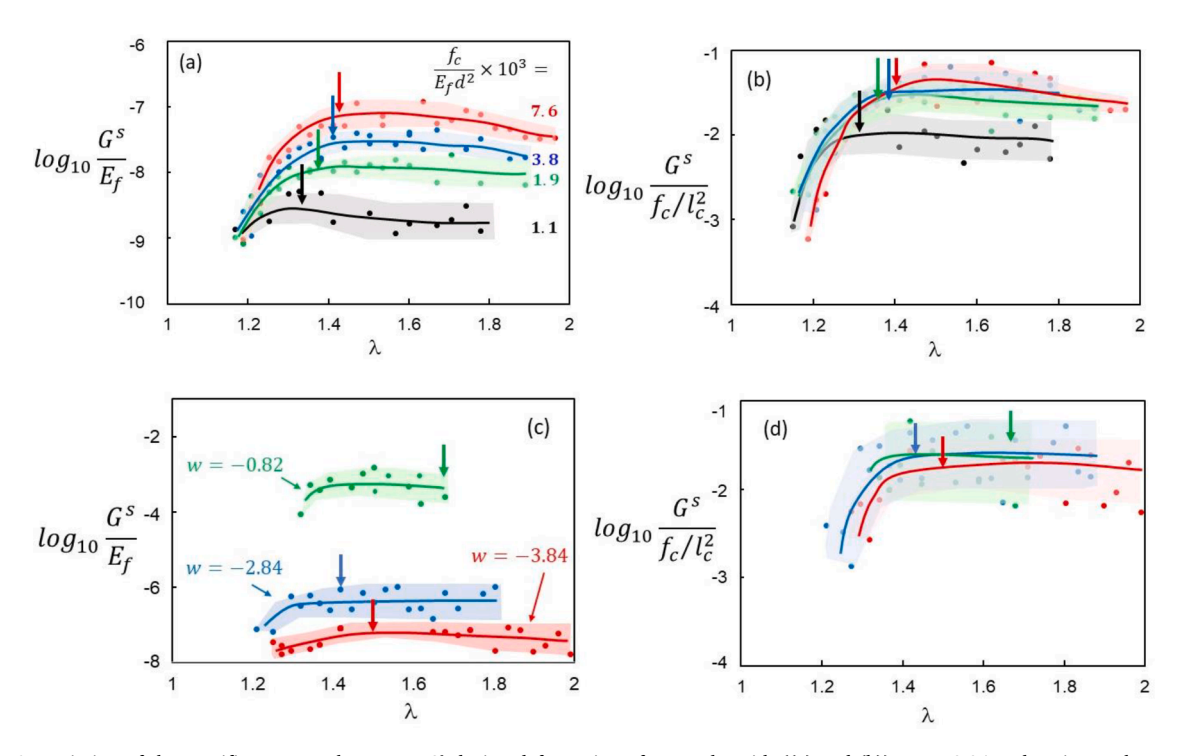


Fig. 6. Variation of the specific energy release rate G_c^s during deformation of networks with ((a) and (b)) w = -3.84 and various values of the normalized crosslink strength, $f_c/E_f d^2$, considered in Fig. 2, and ((c) and (d)) networks with w = -3.84, -2.84 and -0.82 considered in Fig. 4. (a) and (c) show G_c^s normalized by E_f (E_f is identical for all systems considered), while (b) and (d) show G_c^s normalized by f_c/f_c^2 . The points represent values obtained with one realization, the shades show the range of fluctuations and the lines show the means. The vertical arrows indicate the position of peak stress.

network toughness, $G = G_c$, which is taken as a material property. One infers that the values shown in Fig. 6 are actually G_c^s and then the network toughness scales linearly with *UTS*, i.e.

$$G_c^s \sim \frac{f_c}{l^2} \sim UTS \sim \rho_b f_c(\zeta l_c)$$
 (4)

The length parameter required by dimensional considerations in Eq. (4), ζl_c , is expressed in units of l_c . The coefficient of proportionality in the relation $G_c^s \sim f_c/l_c^2$ that results from Fig. 6b and d is approximately 0.03. With the data in Fig. 3, this implies that $G_c^s \approx UTS/3$ for the present networks.

It is of interest to compare Eq. (4) with the Lake-Thomas theory which relates the fracture toughness of molecular networks to the network parameters. As indicated in the Introduction, the Lake-Thomas model applies to the growth of cracks and provides the energy required to rupture the molecular strands penetrating the crack plane. If a force f_c is required to rupture a strand or a crosslink, and the number density of strands penetrating any plane that cuts the solid is $\rho_\#^{2D}$, the toughness results $G_c^{LT} = \rho_\#^{2D} f_c L^*$, where the length L^* is required for dimensional consistency. The number density $\rho_\#^{2D}$ may be written in terms of the crosslink density ρ_b by considering that the number density of strands in 3D is $\rho_\#^{3D} = \rho_b \overline{z}/2$; then, $\rho_\#^{2D} = \rho_\#^{3D} l_c = \rho_b \overline{z} l_c/2$. Note that when fiber segments are not straight, $\rho_\#^{2D} = \rho_\#^{3D} \xi$, where ξ is the mean end-to-end distance of segments or the mesh size; in the present case $\xi = l_c$ since fiber segments are straight. Therefore, the Lake-Thomas energy release rate may be written as:

$$G_c^{IT} \sim \rho_b \overline{z} f_c l_c L^*$$
 (5)

 L^* is a parameter which is typically fitted to the experimental data. However, it may be attributed a physical meaning. In order to develop in a molecular strand the rupture force, f_c , it is necessary to stretch the strand tight. The length L^* may be thought of as being the difference between the contour length of the strand and its end-to-end length in the undeformed configuration. This situation is contrasted with the physical picture underlying Griffith's theory, case in which relative displacements of the order of the interatomic spacing need to be applied to separate atoms on the two sides of a crack. Clearly, the work performed to create the unit area of crack surface is much larger in the molecular network than in the brittle solid case since L^* is much larger than the interatomic spacing.

Eq. (4) has the same structure with the Lake-Thomas equation, Eq. (5). As indicated above, since no pre-existing crack exists in the present case, the units of the critical specific energy release rate G_c^s are J/m^3 , while the energy release rate associated with the growth of a crack, G_c^{LT} , has units of J/m^2 . Other than this difference which emerges from the definition of the two quantities, the two expressions are identical. The present results extend the Lake-Thomas theory to athermal networks and to materials without pre-existing cracks in which the network ruptures gradually.

We note that the observation that the network ruptures at constant G^s applies in the regime in which damage accumulates gradually. When damage localizes and a major crack forms, G^s defined here increases abruptly and the energy release rate used in fracture mechanics should be used.

Other dissipation mechanisms not considered in this work may contribute to the material toughness, and may even become dominant, in some network materials. Inter-filament friction produces dissipation and rate effects in polymeric networks. Friction of nanofibers may be considered viscous, (Das and Chastiotis, 2020) while friction between filaments of diameter larger than micron (e.g. in nonwovens) is generally Coulombic. In either case, this mechanism is important only in networks of low free volume such as rubber, entangled polymeric melts and dense nonwovens. Additional dissipation mechanisms may be activated if the network is embedded in a viscoelastic or viscoplastic matrix, as is the case with most biological tissue.

4. Conclusions

This study focuses on the rupture of stochastic network materials in the regime in which damage accumulates gradually leading to material softening. Crosslinks fail both before and after peak stress at rates that reach maximum values at the peak stress. The energy released per crosslink failure has two components, one associated with the separation of the crosslink and the other associated with the release of stored strain energy; the second component is much larger than the first. It is observed that the global rate of energy release is constant during the regime of incremental damage accumulation, which leads to the inference of a toughness measure applicable to materials without pre-existing cracks. This intrinsic network toughness is proportional to the ultimate tensile strength and scales linearly with the crosslinks strength and inversely with the square of the mean segment length. Although the toughness measure proposed here is different from that commonly used in fracture mechanics, the relation derived between the present toughness and network parameters is similar to the Lake-Thomas model developed for thermal molecular networks and applicable to crack growth situations. Therefore, the present work extends the Lake-Thomas theory to cases without pre-existing cracks in which damage accumulates incrementally.

Declaration of Competing Interest

The authors declare that they have no known competing financial interests or personal relationships that could have appeared to influence the work reported in this paper.

Data availability

Data will be made available on request.

Acknowledgement

Picu, R.C., 2011. Soft Matter 7, 6768.

This work was supported by the National Institutes of Health (NIH) through Grant No. U01 AT010326-06 and by the National Science Foundation (NSF) though Grant CMMI-2007909.

References

```
Alava, M.J., Niskanen, K., 2006. Rep. Prog. Phys. 69, 669.
Alava, M.J., Nukala, P.K.V.V., Zapperi, S., 2008. Phys. Rev. Lett. 100, 1.
Alava, M.J., Nukala, P.K.V.V., Zapperi, S., 2008. Int. J. Fract. 154, 51.
Amjad, S.N., Picu, R.C., 2022. Soft matter 18, 446.
Arcangelis, L., de Hansen, A., Herrmann, H.J., Roux, S., 1989. Phys. Rev. B 40, 877.
Bancelin, S., Lynch, B., Bonod-Bidaud, C., Ducourthial, G., Psilodimitrakopoulos, S., Dokladal, P., Allain, J.M., Schanne-Klein, M.C., Ruggiero, F., 2015. Sci. Rep. 5,
Bazant, Z.P., Tabbara, M.R., Kazemi, M.T., Pyaudier-Cabot, G., 1991. J. Eng. Mech. 116, 1686.
Bergstrom, P., Hossain, S., Uesaka, T., 2019. Int. J. Sol. Struct. 166, 68.
Berthier, E., Kollmer, J.E., et al., 2019. Phys. Rev. Mat. 3, 075602.
Bonamy, D., 2009. J. Phys. D.- Appl. Phys 42, 1.
Borodulina, S., Kulachenko, A., Galland, S., Nygards, M., 2012. Nordic Pulp. Paper Res. J. 27, 318.
Borodulina, S., Motamedian, H.R., Kulachanko, A., 2018. Int. J. Sol. Struct. 154, 19. Chen, N., Koker, M.K.A., Uzun, S., Silberstein, M.N., 2016. In-situ X-Ray study of the deformation mechanisms of non-woven polypropylene. Int. J. Sol. Struct. 97-98,
Curtin, W.A., 1998. Phys. Rev. Lett. 80, 1445.
Daguier, P., Nghiem, B., Bouchaud, E., Creuzet, F., 1997. Phys. Rev. Lett. 78, 1062.
Das, D., Chastiotis, I., 2020. J. Mech. Phys. Sol. 140, 103931.
Deogekar, S., Islam, M.R., Picu, R.C., 2019. Int. J. Sol. Struct. 168, 194.
Deogekar, S., Picu, R.C., 2018. J. Mech. Phys. Sol. 116, 1. Deogekar, S., Picu, R.C., 2021. Soft Matter 17, 704.
Deogekar, S., Yan, Z., Picu, RC., 2019. J. Appl. Mech. 86, 081010.
Driscoll, M.M., Chen, B.G., Beuman, T.H., Ulrich, S., Nagel, S.R., Vitelli, V., 2016. Proc. Nat. Acad. Sci. 113, 10813.
Dussi, S., Tauber, J., van der Gucht, J., 2020. Phys. Rev. Let. 124, 018002.
Eriksson, M., Torgnysdotter, A., Wagberg, L., 2006. Ind. Eng. Chem. Res. 45, 5279.
Fang, J., Li, H., 2012. Langmuir 28, 8260.
Forsstrom, J., Torgnysdotter, A., Wagberg, L., 2005. Nordic Pulp Paper Res. J. 20, 186.
Fukasawa, M., Sakai, T., Chung, U., Haraguchi, K., 2010. Macromolec. 43, 4370.
Gent, A.N., Lindley, P.B., 1959. Proc. R. Soc. London 249A, 195.
Gent, A.N., Tobias, R.H., 1982. J. Polym. Sci. Polym. Phys. Ed. 20, 2051.
Goutianos, S., Mao, R., Peijs, T., 2018. Int. J. Sol. Struct. 136-137, 271.
Hansen, A., Hinrichsen, E.L., Roux, S., 1991. Phys. Rev. Lett. 66, 2476.
Hatami-Marbini, H., Picu, R.C., 2008. Phys. Rev. E 77, 062103.
Head, D.A., Levine, A.J., MacKintosh, F.C., 2003. Phys. Rev. E 68, 061907.
Herrmann, H.J., Hansen, A., Roux, S., 1981. Phys. Rev. B 39, 637.
Heussinger, C., Frey, E., 2006. Phys. Rev. Lett. 97, 105501.
Heyden, S., 2000. Network Modelling for the Evaluation of Mechanical Properties of Cellulose Fiber Fluff PhD Thesis. Lund University. Lund, Sweden.
Heyden, S., Gustafsson, P.J., 1998. J. Pulp Paper Sci. 25, 160.
Huang, C.Y., Stankiewicz, A., Ateshian, G.A., Mow, V.C., 2005. J. Biomech. 38, 799.
Isaksson, P., Hägglund, R., 2007. Int. J. Solids Struct. 44, 6135.
Islam, M.R., Picu, R.C., 2018. J. Appl. Mech. 85, 801011.
Jagota, A., Bennison, S.J., 1994. In: Non-Linearity and Breakdown in Soft Condensed Matter. Springer, Berlin, Heildelberg, p. 186.
Jang, W.Y., Kraynik, A.M., Kyriakides, S., 2008. Int. J. Solids Struct. 45, 1845.
Jerauld, G.R., Scriven, L.E., Davis, H.T., 1984. J. Phys. C: Solid State Phys. 17, 3429.
Kabla, A., Mahadevan, L., 2007. J. R. Soc. Interface 4, 99.
Koh, C.T., Strange, D.G.T., Tonsomboon, K., Oyen, M.L., 2013. Acta Biomater 9, 7326.
Kulachenko, A., Uesaka, T., 2012. Mech. Mater. 51, 1.
Lake, G.J., Lindley, P.B., 1964. Rubber J. 146, 24.
Lake, G.J., Lindley, P.B., 1965. J. Appl. Poly. Sci. 9, 1233.
Lake, G.J., Thomas, A.G., 1967. Proc. R. Soc. London 300, 108.
Li, J., Suo, Z., Vlassak, J.J., 2014. J. Mater. Chem. B2, 6708.
Licup, A.J., Sharma, A., MacKintosh, F.C., 2016. Phys. Rev. E 93, 021407.
Mai, T.T., Matsuda, T., Nakajima, T., Gong, J.P., Urayama, K., 2018. Macromolec 51, 5245.
Malakhovsky, I., Michels, M.A.J., 2007, Phys. Rev. B 76, 1.
J.M. Malho, C. Ouellet-Plamondon, M. Ruggeberg, P. Laaksonen, O. Ikkala, I. Burgert and M.B. Linder. Biomacromolec. 2015,16, 311.
Mao, R., Goutianos, S., Tu, W., Meng, N., Tang, G., Berglund, L.A., Peijs, T., 2017. J. Mater. Sci. 52, 9508.
Mauri, A., Ehret, A.E., Perrini, M., Maake, C., Ochsenbein-Kolble, N., Ehbar, M., Oyen, M.L., Mazza, E., 2015. J. Biomech. 48, 1606.
Meng, L., Arnoult, O., Smith, M., Wnek, G.E., 2012. J. Mater. Chem. 22, 19412.
Normand, V., Lootens, D.L., Amici, E., Plucknett, K.P., Aymard, P., 2000. Biomacromolec. 1, 730.
Ovaska, M., Betalan, Z., Misksic, A., et al., 2017. J. Mech. Beh. Biomed. Mater. 65, 42.
Oyen, M.L., Cook, R.F., Calvin, S.E., 2004. J. Mater. Sci. 15, 651.
Pal, A., Picu, R.C., 2017. Phys. Rev. Lett. 119, 085502.
Patel, P.C., Kothari, V.K., 2001. Indian J. Fibr. Text. Res. 26, 409.
```

R.C. Picu and S. Jin

Picu, R.C., 2022. Network Materials: Structure and Properties. Cambridge Univ. Press.

Picu, R.C., Deogekar, S., Islam, M.R., 2018. J. Biomech. Eng. 140, 21002.

Popil, R.E., 2017. The Physical Testing of Paper. Smithers Group Company, Shrewsbury, UK.

Purslow, P.P., 1985. Meat Science 12, 39.

Rawal, A., Patel, S.K., Kumar, V., Saraswat, H., Sayeed, M.M.A, 2013. Textile Res. J. 83, 1103.

Rosti, J., Illa, X., Koivisto, J., Alava, M.J., 2009. J. Phys. D. Appl. Phys. 42.

Rosti, J., Salminen, L.I., Seppala, E.T., Alava, M.J., Niskanen, K.J., 2001. Eur. Phys. J. B19, 259.

Roux, S., Vandembroucq, D., Hild, F., 2003. Eur. J. Mech. A/Solids 22, 743.

Schmied, F.J., Teichert, C., Kappel, L., Hirn, U., Bauer, W., Schennach, R., 2013. Sci. Reports 3, 2432.

Sherman, V.R., Yang, W., Meyers, M.A., 2015. J. Mech. Beh. Biomed. Mater. 52, 22.

Shi, L., Long, K., Zhong, Y., Luo, G., Ma, X., Li, M., He, X., Yu, J., 2020. J. Eur. Ceram. Soc. 40, 115.

Shulmeister, V., van der Burg, M.W.D., van der Giessen, E., Marissen, R., 1998. Mech. Mater. 30, 125.

Stachewicz, U., Peker, I., Tu, W., Barber, A.H., 2011. ACS Appl. Mater. Interfaces 3, 1991.

Stok, K., Oloyede, A., 2007. Clinical Biomech 22, 725.

Tutwiler, V., Singh, J., Litvinov, R.I., Bassani, J.L., Purohit, P.K., Weisel, J.W., 2020. Sci. Adv. 6, 1–8 eabc0496.

Waddoups, M.E., Eisenmann, J.R., Kaminski, B.E., 1971. J. Compos. Mater 5, 446.

Zagar, G., Onck, P.R., van der Giessen, E., 2015. Biophys. J. 108, 1470.

Zhang, L., Lake, S.P., Barocas, V.H., Shephard, M.S., Picu, R.C., 2013. Soft Matter 9, 6398.

Zhang, L., Rocklin, D.Z., et al., 2017. Phys. Rev. Mat. 1, 052602(R).